Progress In Electromagnetics Research B, Vol. 34, 31–46, 2011

ENHANCED POLARIZATION IN TADPOLE-SHAPED (NI, AL)/ALN NANOPARTICLES AND MICROWAVE ABSORPTION AT HIGH FREQUENCIES

H. Huang[1], F.-H. Xue[1], B. Lu[1], F. Wang[1], X.-L. Dong[1,*], and W.-J. Park[2]

[1]School of Materials Science and Engineering, Dalian University of Technology, Dalian, Liaoning 116024, China

[2]School of Mechanical and Aerospace Engineering, Gyeongsang National University, Inpyeong-Dong 445, Tongyoung, Gyeongsangnamdo 650-160, South Korea

Abstract—Tadpole-shaped (Ni, Al)/AlN nanoparticles were synthesized via evaporating Ni-Al alloy in a mixed atmosphere of N_2 and H_2. As a counterpart, the spherical-shaped (Ni, Al)/Al_2O_3 nanoparticles were also prepared from the same target alloy while in a mixture of Ar and H_2. The electromagnetic parameters of as-made nanoparticles/paraffin composites were then investigated in the frequency range of 2–18 GHz. Excellent microwave absorption can be obtained for the tadpole-shaped (Ni, Al)/AlN-paraffin composite at high frequencies and in a thin layer, which is thought to be the result of the enhanced polarization in the anisotropic tadpole-shaped nanoparticles. With the increasing of the composite thickness, the frequency of effective reflection loss shifts towards lower frequencies due to an improved impedance match and absorption.

1. INTRODUCTION

Microwave absorbing materials are widely used to provide the electromagnetic solutions in military shielding and commercial electronics including wireless LAN devices, global positioning system, target-acquisition radar and other high-frequency devices. Theoretically, a perfect absorber should own high dielectric and magnetic loss, as well as impedance match [1] to achieve effective

Received 11 July 2011, Accepted 22 August 2011, Scheduled 30 August 2011

* Corresponding author: Xing Long Dong (dongxl@dlut.edu.cn).

absorption in a thin layer possible. As one kind of absorbents, 3d-transition metals or alloys have attractive advantages for their novel magnetic properties and high Snoek's limit in GHz range. However, the permittivity (ε) and permeability (μ) of pure metals are often hard to be adjusted to suit the requirements of the impedance match. Diverse dielectric materials such as oxides [2, 3], carbon [4] and polymers [5, 6] are consequently introduced on the metal nanoparticle surface, forming metal-dielectric composite structure. Such nanostructure provides practical routes in tailoring the electromagnetic properties and impedance match. Further, the charge accumulation at metal-dielectric interfaces produces extra polarizations and new-generated dipoles, which can always bring enhanced electromagnetic loss [7].

Aluminum nitride (AlN), as one of the III-V nitride-based semiconductors, owns unique physical properties such as wide band gap, high thermal conductivity (0.823–2.0 $\mathrm{Wcm^{-1}K^{-1}}$) and good mechanical strength [8, 9]. Recently, AlN nanomaterials are of fresh interests due to their high surface area, low dimensionality and dramatically improved performance for many applications, such as in the field-emission and light-emitting nanodevices [10, 11]. Various types of AlN nanostructures with controlled high-aspect-ratio shapes of wires, cones, tips, or belts, have been successfully synthesized by diverse techniques including CVD process [11], direct nitridation [10], or arc-discharge method [12]. In this work, we present a first report of tadpole-shaped (Ni, Al)/AlN nanoparticles synthesized by modified arc-discharge method. The as-synthesized nanoproduct has a metallic (Ni, Al) head attached by a well-crystallized AlN tail. Several considerations have been paid for the selection of AlN to form composite with Ni nanoparticles. i) AlN is an excellent electromagnetic loss material as its own dielectric properties [13]. It has attracted special commercial interests to replace the toxic beryllium oxide (BeO) ceramics in microelectronics applications and high-frequency integrated devices [14]. ii) The anisotropic shapes of AlN nanostructures are benefit to the generation of electric dipoles and the enhancement of dipole moments. The combination of AlN and Ni in nanoscales can also adjust the dielectric and magnetic properties for a better impedance match. iii) AlN has high temperature resistance with a sublimation temperature of 2200°C. As the shell, AlN can prevent the Ni nanocores from oxidation and ensure chemical stability of the composite nanoparticles.

2. EXPERIMENTAL

The tadpole-shaped (Ni, Al)/AlN nanoparticles were prepared by modified arc-discharge method, as it is used in our former work [15]. Firstly, a binary-alloy ingot was prepared by arc melting Ni and Al blocks ($> 99.9\%$ in purity) in a molar ratio of $3:1$. In the arc-discharge process, the ingot is served as the anode and a tungsten rod as the cathode. N_2 (99.999% in purity) of 2×10^4 Pa was then introduced into the evacuated chamber as a reactive gas together with H_2 of 2×10^4 Pa as a source of hydrogen plasma. After the evaporation of target alloy, the powder products were stabilized for 5 hours, and then passivated with a small amount of air. The nano powder was collected on the chamber walls. For comparison, a counterpart specimen of (Ni, Al)/Al_2O_3 nanoparticles was also prepared by evaporating the same target alloy in a mixture of H_2 (2×10^4 Pa) and Ar (2×10^4 Pa).

The structures of nanoparticle were characterized by XRD with Cu Kα radiation and their morphologies were inspected by HRTEM (Tecnai G220 S-Twin). A photoluminescence (PL) spectrum for the nanoparticles was obtained using a KIMMON IK3301R-G spectrometer at room temperature. The 325 nm line of a He-Cd laser (30 mW in power) was used as the excitation source. For the microwave measurement, 40 wt.% as-made nanoparticles were homogeneously blended into a melted paraffin matrix. After hardening, the mixture was die-pressed into toroidal compacts with 7.00 mm outer diameter and 3.00 mm inner diameter. The toroidal material has the same thickness of 2 mm with the compact and the error of the thickness was controlled within 0.05 mm by fine grinding of the surface. The toroid was then tightly fit into a coaxial measurement cell. On the test setup, full two-port calibration was initially performed in order to remove errors due to the directivity, source match, load match, isolation and frequency response in both the forward and reverse measurements. The scattering parameters corresponding to the reflection (S_{11} and S_{22}) and transmission (S_{21} and S_{12}) were measured in the frequency range of 2–18 GHz by an Agilent 8722ES network analyzer. The complex permeability and permittivity were determined from the scattering parameters using the Nicolson-Ross (for magnetic) and precision (for nonmagnetic) models [16], which are included in the Agilent measurement software and have the declared accuracy within 2%.

3. RESULTS AND DISCUSSION

X-ray diffraction pattern of as-prepared nanoparticles is shown in Figure 1. The diffraction peaks of (Ni, Al)/AlN nanoparticles in Figure 1(a) are indexed to Ni, Ni_3Al and AlN phases. The strong intensity of the Ni peaks indicates that Ni is the main phase in the (Ni, Al)/AlN nanoparticles. The peaks at 35.59°, 60.05° and 72.02° correspond to AlN (111), (220) and (311) planes (JCPDS 87-1053) and indicate that AlN we obtained has a face-centered-cubic (FCC) structure with the lattice constant of $a = 4.318$Å on the JCPDS card. There are no detectable reflections for Al, suggesting that Al has been exhausted out to construct the compounds during the particle formation. As the counterpart, (Ni, Al)/Al_2O_3 nanoparticles have the same diffraction peaks for the components of Ni and Ni_3Al. However instead of AlN, the phase of α-Al_2O_3 can be found from the peaks of 25.6°, 35.2° and 37.70°, corresponding to its (012), (104) and (110) planes (JCPDS 88-0826) respectively.

The morphology of (Ni, Al)/AlN nanoparticles is given in Figure 2(a), which shows a tadpole-like shape of the nanoparticles. More details are given in Figure 2(b), a HRTEM image of the tail. This image indicates that the tail is a single crystal with interplanar spacing of 0.253 nm between the neighboring lattice planes, which agrees with the $d_{(111)}$ space of c-AlN in the XRD analysis. A thin amorphous layer surrounding the outer surface of the whole nanoparticle was also observed with the thickness about $3 \sim 4$ nm, which may come from the surface oxidation in air or just the less crystallized nitrides. Figure 2(c) presents the morphology of (Ni, Al)/Al_2O_3 nanoparticles

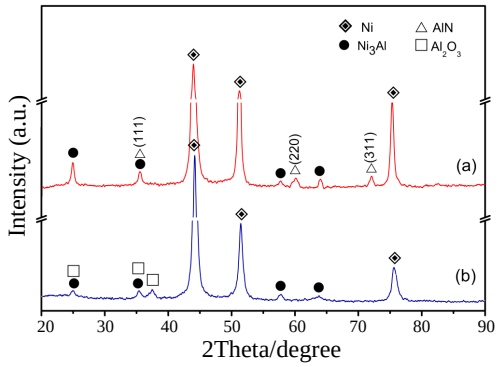

Figure 1. XRD pattern of as-prepared nanoparticles: (a) (Ni, Al)/AlN and (b) (Ni, Al)/Al_2O_3.

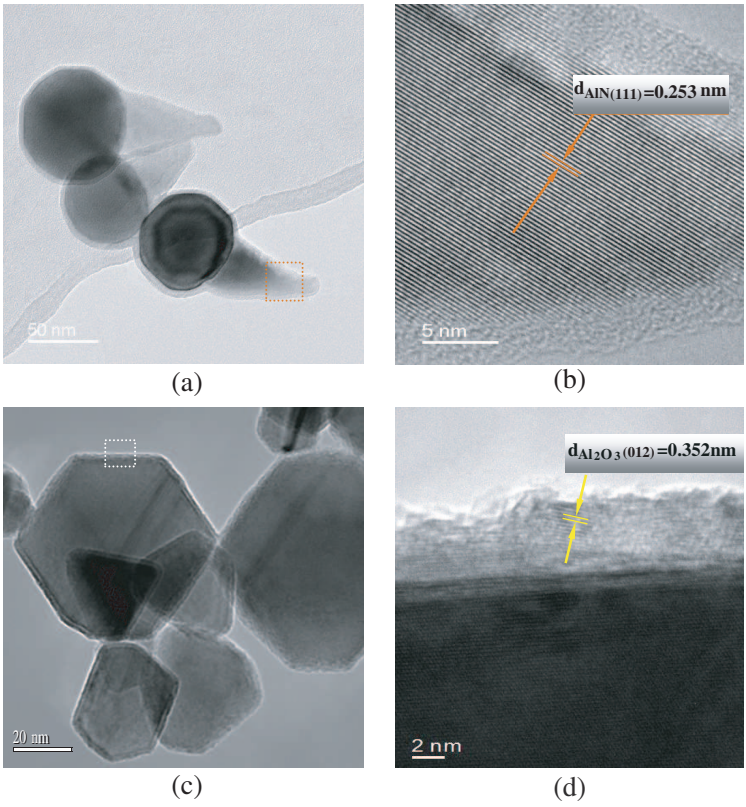

Figure 2. (a) TEM image of (Ni, Al)/AlN nanoparticles, (b) HRTEM image of the region labeled by a dotted rectangle in image (a), (c) TEM image of (Ni, Al)/Al_2O_3 nanoparticles, (d) HRTEM image of the region labeled by a dotted rectangle in image (c).

with polygonal shapes. Their size ranges from 30 nm to 80 nm. The rectangle region labeled in Figure 2(c) is magnified for the details of the core-shell nanoparticle (Figure 2(d)). The shell of nanoparticles is identified as a crystallized α-Al_2O_3 with the interplanar spacing of 0.352 nm which refers to α-Al_2O_3 (012) planes.

In the arc-discharge process of preparing (Ni, Al)/AlN nanoparticles, Ni-Al bulk alloy is firstly evaporated along with the nitrogen radicals in a N_2 atmosphere. The atoms of Ni and Al coexist in a gaseous state when the temperature is above the boiling point of Ni ($T_{b,Ni}$ = 2913°C) and Al ($T_{b,Al}$ = 2519°C). By the vapor-liquid-solid (VLS) model [17, 18], the vapor of Ni and Al will then condense into Ni-rich liquid droplets between the temperatures of $T_{b,Al}$ and $T_{m,Ni}$

(melting point of Ni, $T_{m,Ni}$ = 1455°C). Simultaneously, the Al-N species may nucleate at interfaces. As the temperature decrease below $T_{m,Ni}$, Ni droplet solidifies into the metal cores of nanoparticles, along with the growth of *c*-AlN at the interfaces. As we know, AlN has two main crystal structures: hexagonal wurtzite (α-phase *h*-AlN) and cubic zincblende (β-phase *c*-AlN). Although the α- and β-phases of AlN only differ in the stacking sequence of nitrogen and Al atoms, the preparation of α-phase AlN is much easier than that of the β-phase. If pure Al block is evaporated in N_2 atmosphere by the same arc-discharge method, the crystal of the AlN products is wurtzite structure only [12]. Recently, *c*-AlN attracts increasing interests and it is expected to possess higher ballistic electron velocities and thermal conductivity because of its higher crystallographic symmetry than that of *h*-AlN [19]. Due to its metastable character, the *c*-AlN is always fabricated with the assistant of catalyst or grows on certain substrate [17]. In our case, the formation of *c*-AlN is considered as the contributions of the pre-condensed Ni nanocores. Figure 3 is the HRTEM image taken at the junction of the metallic head and AlN tail. It can be observed that *c*-AlN grows along the [111] crystal orientation of Ni nanocore that also has a FCC structure. The surface of pre-condensed metallic Ni provides vicinal (111) planes and acts as the catalytic active site for the nucleation and the subsequent growth of the *c*-AlN. Beside the reaction with N atoms, Al also combines Ni into the Ni_3Al intermetallic compound through interface reaction and diffusion. It has been experimentally found that Ni_3Al emerges as the primary phase in the annealed Ni-Al film with excessive Ni content [20]. The sphere-shaped (Ni, Al)/Al_2O_3 nanoparticles experience the similar growth

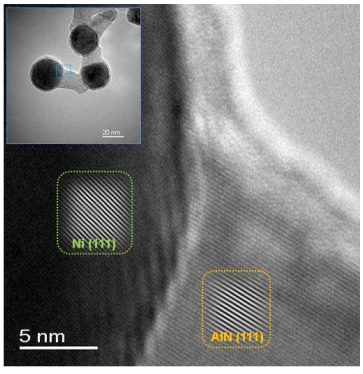

Figure 3. HRTEM image taken at the junction of the head and tail of the tadpole-shaped (Ni, Al)/AlN nanoparticles in the insert.

mode of physical evaporation and condensation, however the Al_2O_3 shell is formed around the nanoparticles in the succedent process of passivation, as indicated in XRD spectrum and HRTEM image.

The photoluminescence (PL) spectra of the (Ni, Al)/AlN and (Ni, Al)/Al_2O_3 nanoparticles is collected and shown in Figure 4. It is can be seen a broad UV-blue emission band centered at 350 nm (i.e., 3.54 eV, converted by $E = hc/\lambda$, where h is Planck's constant, c is the speed of light) in the curve for (Ni, Al)/AlN. This band is clearly not the direct band gap emission of AlN (6.3 eV), but it is referred to a deep- or trap-level state. It was previously proposed [21] that the oxygen related defects in AlN nanostructures, such as nanorods or nanotips, are responsible for the UV-blue emission around 3.5 eV. The hole part of the luminescence center is formed by the defects of an Al vacancy (v_{Al}) together with a close oxygen substituting for nitrogen (O_N), resulting in the (v_{Al}-O_N) pair formation. Another closely neighbored oxygen (O_N) can act as the electron part and transformed into the $(O_N)^-$ center after it capture an electron. Accordingly, the (v_{Al}-O_N) center losses an electron and transforms into the $(v_{Al}\text{-}O_N)^+$ center containing a trapped hole. The combination of the $(v_{Al}\text{-}O_N)^+$ and $(O_N)^-$ centers with emission of a light quantum results in the UV-blue luminescence around 3.5 eV. Furthermore, the maximum position of the UV-blue PL band varies within the spectral range of 350 nm–420 nm, depending on the concentration of the oxygen-related defects in nanostructured AlN materials. It was demonstrated that the UV-blue luminescence varies from 350 nm up to 380 nm when the oxygen concentration increases

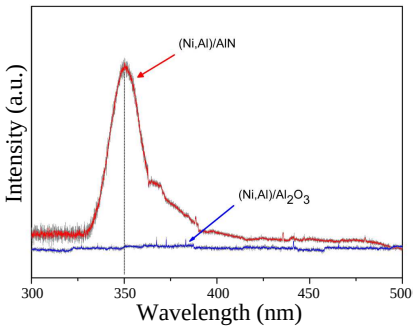

Figure 4. Photoluminescence spectra of the (Ni, Al)/AlN and (Ni, Al)/Al_2O_3 nanoparticles.

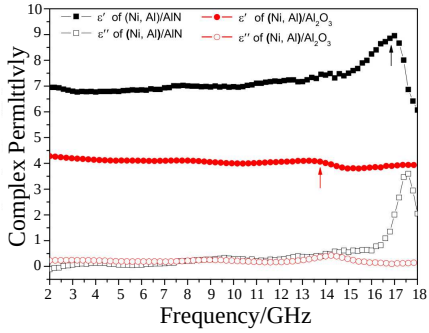

Figure 5. Frequency dependences of complex permittivities for the paraffin composite with (Ni, Al)/AlN and (Ni, Al)/Al_2O_3 nanoparticles.

from 0.3 up to 0.75 atomic percent in AlN ceramics [22]. Hence, the luminescence at 350 nm of our (Ni, Al)/AlN nanoparticles originates from the co-work of oxygen-related defect and Al vacancy in weakly oxided aluminum nitrides, while we cannot find any PL response in the (Ni, Al)/Al_2O_3 nanoparticles. Photoluminescence spectra of the nanoparticles definitely confirmed the presence of (Ni, Al)/AlN, moreover, oxygen-related defects and interfaces of the nanoparticles can provide additional polarization due to their charge accumulation at the defects and the interfaces.

Figure 5 shows the frequency dependence of the real parts (ε') and imaginary parts (ε'') of complex permittivities for the (Ni, Al)/AlN and (Ni, Al)/Al_2O_3 nanoparticles. The ε' and ε'' values of (Ni, Al)/AlN nanoparticles are almost constants of 7 and 0.25 respectively in the range of 2–15 GHz, while those of (Ni, Al)/Al_2O_3 nanoparticles are 4.0 and 0.22 respectively in the same frequency range. Overall, the complex permittivities of the prepared samples are lower than those of the ferromagnetic metal nanoparticles. In our former reports, the ε' value of the paraffin matrix composites containing Fe nanoparticles is about 16 and that of Ni nanoparticle was measured around 14 over 2–18 GHz [23]. Metal alloy nanoparticles always show lower real permittivity than corresponding mono metals. For example, CoFe alloy nanoparticles were reported to have the ε' values around 6.5 in the frequency range of 2–14 GHz [24]. The permittivity of $FeNi_3$ alloy particles is almost constant of 5.9 in the 2–10 GHz range [25] that is nearly half lower than that of Fe and Ni nanoparticles. It is speculated that the lower ε' values of these alloys result from the increasing resistivity, because metal alloys normally have greater resistivity than pure metals. As tested in the deposited Ni-25Al film [26] by magnetron sputtering, the nanofilm has the resistivity around 20 MΩ at 300 K, which is obviously higher than that of pure Ni or Al.

For present samples, higher ε' values of (Ni, Al)/AlN than that of (Ni, Al)/Al_2O_3 can also be observed in Figure 5. Generally, the real part of permittivity is an expression of the polarization ability of a material. Hence, higher ε' values of (Ni, Al)/AlN are thought as the result of the enhanced interfacial polarization originated from the charge accumulation at the heterogeneous interface of Ni and AlN. We notice that the difference of work functions (AlN: 3.70 eV [27]; Ni: 5.15 eV [28]) leads to the existence of contact potential at the AlN-Ni interface and results in a redistribution of charges. The electric double layer is formed at the AlN-Ni interface as described in a previous work [29]. A recent research [30] further indicated that metals in a dielectric matrix can greatly affect the polarizability of the surrounding ions and benefit the increasing of born effective charges for the double

layers. Further, the interfacial polarization can also be enhanced owe to small electron affinity of AlN, ranging from negative values to 0.6 eV [31]. Electrons can easily escape at the interface with such a small electron affinity when an electric field is applied. As a result, higher real permittivity of (Ni, Al)/AlN nanoparticles can be obtained in the full frequency range and it indicates an additional relaxation constructed at the Ni-AlN interfaces.

In the frequency range of 15–18 GHz, it appears an obvious peak in the ε' curve of (Ni, Al)/AlN. It is obviously that this strong peak cannot be found either in Ni-Al alloy or in AlN [14]. The (Ni, Al)/AlN nanoparticle is a such perfect system, because the metallic-dielectric nanocomposite with the polarized charges can play the role of dipoles, as demonstrated in the silver nanoparticles dispersed in an aluminum oxide thin film [32]. When applied signal frequency is much lower than the relaxation frequency of the nanoparticles, such as in the KHz to MHz range [33], the dipoles will be polarized and contribute to the overall permittivity of the nanocomposite. However in the microwave region, the applied frequency is beyond the dipole relaxation frequency so that the electrons in the dipoles do not have sufficient time to response the alternations of the electric field [34], while just vibrate at their positions. Resonance will happen at certain frequency as it is found at around 17 GHz in (Ni, Al)/AlN sample. Another important contribution to the intensive resonance of dipoles comes from the asymmetric topology of in-particle structure. The anisotropic shape of tadpole-like (Ni, Al)/AlN nanoparticles can produce potentially significant induced and/or permanent dipole moments, as appeared in the nanowires [35] and fibers [36]. It is the same reason why the ZnO nanowires have stronger microwave absorptions than the ZnO microparticles [37]. Actually we can also find a peak at about 14 GHz in the real permittivity curve of (Ni, Al)/Al_2O_3, as indicated by arrow in Figure 5. However, its weaker intensity than that of (Ni, Al)/AlN may be related to a lower accumulated charge density or electric dipole moments.

The complex permeability of (Ni, Al)/AlN nanoparticles is plotted in Figure 6. The real part remains an approximate constant of about 1.2 over 2–18 GHz, and the imaginary part slowly increases from 0 to 0.27 with frequency increasing. Generally the relative permeability can be expressed as $\mu = 1 + (M/H)$, where M is the magnetization and H is the external magnetic field. According to this basic equation, it is can be seen that the lower permeability values of (Ni, Al)/AlN nanoparticles than that of pure Ni nanoparticles [23] result from the decreasing saturation magnetization of (Ni, Al)/AlN nanoparticles with nonmagnetic ingredients. Several peaks, such as that at 3.2,

6.0 and 11.2 GHz, are observed in the curve of μ''. Generally, the magnetic loss is implied by the imaginary part of permeability and originates mainly from several factors, such as the magnetic hysteresis, domain-wall displacement, eddy current loss and natural resonance. The hysteresis loss normally can be neglected in a weak applied field. The domain-wall resonance occurs only in multi-domain materials and in the 1–100 MHz range [38]. The eddy current loss in the nanoparticles can be effectively suppressed by the outer insulator and reduced particle sizes. Hence, the peaks in the curve of μ'' can be speculated as the multi-resonance attributed to the small size effect, surface effect and spin wave excitations, which have been defined as exchange mode resonance [39]. The resonance frequencies are dependent on the particle's radius and can be observed when reducing the size of the metallic magnetic particles.

Another large variation of permeability can be observed at the frequency range of 16.5–18 GHz. The real permeability increases from 16.5 GHz and reaches to maximum value at 17.5 GHz, which indicates an increase of magnetic energy storage. It is interesting that this variation happens in the same frequency band with that in the permittivity curve. For a better comprehension, the tangent loss ($\tan\delta_\varepsilon = \varepsilon''/\varepsilon'$, $\tan\delta_\mu = \mu''/\mu'$) versus frequency curve, as shown in the inset of Figure 6. In the region of 16.5–18 GHz, the variation of dielectric loss and the magnetic loss keeps consistent; however the tendency is opposite each other, which implies that an energy conversion occurs there. Similar phenomenon has been reported

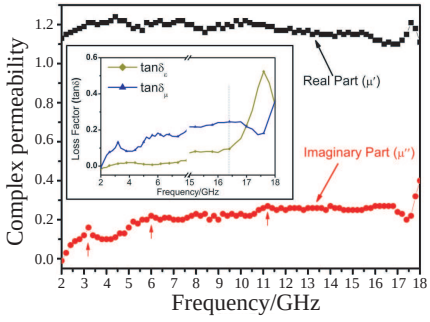

Figure 6. Frequency dependences of complex permeability and tangent loss (insert) for the (Ni, Al)/AlN nanoparticle-paraffin composite.

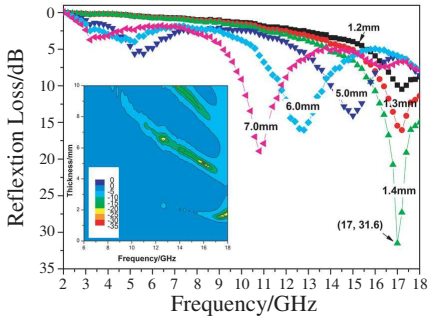

Figure 7. Frequency dependences of reflection loss for (Ni, Al)/AlN nanoparticle-paraffin composite. **Insert**: A contour plot of reflection loss vs. frequency and thickness.

for the Fe_3O_4/ZnO core/shell nanorods and it was speculated that an induced electric current will be produced during the polarization processes due to the semiconductor characteristics of ZnO [37]. In our work, an enhanced polarization also exists at 16–18 GHz as described in the former parts. An induced electric field will formed in our nanoparticles along with the augment of internal magnetic field. As a result, the magnetic energy storage increases with the strong dielectric polarization at high frequencies.

To further reveal the microwave absorption properties of (Ni, Al)/AlN nanoparticles, the reflection loss (RL) were calculated from the measured values of permeability and permittivity. According to the transmission line theory, the RL values can be calculated through the following equations [40]: $RL = 20\log|(Z_{in} - Z_0)/(Z_{in} + Z_0)|$ and $Z_{in} = Z_0(\mu_r/\varepsilon_r)^{1/2}\tanh[j(2\pi ft/c)(\mu_r\varepsilon_r)^{1/2}]$, where t is the thickness of an absorber, c is the velocity of light, Z_0 is the impedance of air, and Z_{in} is the input impedance of absorber. The contour plot of RL vs. frequency and thickness is shown in the insert of Figure 7. Referring to the scale bar, the RL values less than -10 dB, which means over 90% electromagnetic power absorbed, can be found at the high frequency band. The RL curves at selected absorber thicknesses are also plotted in Figure 7. When the thickness increases from 5.0 to 7.0 mm, the optimal RL values move toward the lower frequency region with increasing values. Normally for a microwave absorption curve, the parameters such as peak frequency, absorption intensity (minimum reflection loss) and thickness are always concerned for the evaluation of the absorption performance. However the parameters have inherent relationship with each other. Inui et al. [41] established the quarter-wavelength (l/4) condition for the peak frequency (f_m) and matching thickness (t_m) in the equation, $f_m = nc/(4t_m\sqrt{|\varepsilon||\mu|})$ ($n = 1, 3, 5, 7, 9\ldots$), where c is the velocity of light; ε and μ are complex permittivity and permeability at f_m. This equation can be rewritten into $t_m = \frac{n}{4}\lambda_m$ ($\lambda_m = c/(f_m\sqrt{|\varepsilon||\mu|})$) ($n = 1, 3, 5, 7, 9\ldots$), where λ_m is the propagation wavelength of the microwave in the absorber at f_m. When the thickness of the absorber equals or approaches to $n\lambda_m/4$, the incident and reflected wave are out of phase by π and cancel each other, so that the reflection loss reaches the minimum value. Therefore, we can conclude that the reflection peaks are related to the matching thickness of absorber with the given values of ε and μ. Furthermore, we can also change the value of ε and μ through the fabrication of nanocomposite and adjust the relationship between thickness and reflection peaks.

In the frequency range of 16.5–18 GHz, the optimal RL values decrease from -10 dB to -31 dB with the thickness increasing from

1.2 mm to 1.4 mm. As dedicated in the Figure 7, the minimum RL value of −31.6 dB at 17 GHz is obtained, corresponding to 99.9% microwave absorption in quite a thin layer of 1.4 mm. For a single layered absorber, RL generally arises from dielectric loss, magnetic loss or impedance matching. The magnetic loss is in such a low value at 17 GHz and cannot be the reason for the strong RL. The impedance matching condition requires the intrinsic wave impedances of the absorber (η) equivalent to that of air (Z_0), which can be computed by [42]: $\eta = \sqrt{\mu_0/\varepsilon_0}\sqrt{\mu_r/\varepsilon_r} = Z_0\sqrt{\mu_r/\varepsilon_r}$, where $Z_0 = 377\,\Omega$ and ε_r, μ_r are the complex permittivity and complex permeability of the absorber. According to the equation, the impedance matching condition can be satisfied when μ_r equals to ε_r. By comparing the values in Figures 5 and 6, the permittivity has a large difference with the permeability at 17 GHz, which is far from the impedance matching. Hence, at high frequencies over 16.5 GHz, the strong microwave absorption comes from the strong dielectric loss due to the enhanced polarization in the (Ni, Al)/AlN nanoparticles. While in the range of 2–16.5 GHz, the dielectric loss is comparable with the magnetic loss and both of them contribute to the microwave absorption enhancement in the composite. The optimized RL performance results from a better impedance match between the dielectric and magnetic properties.

4. CONCLUSION

The (Ni, Al)/AlN nanoparticles were fabricated by the arc-discharge method and confirmed to have an unique tadpole-shape nanostructure of (Ni, Al) metallic head and AlN tail. The nanoparticles present strong dielectric loss in the frequency range of 16–18 GHz, which is considered as the result of enhanced interfacial and dipolar polarization, relating to the anisotropic shape of (Ni, Al)/AlN nanoparticles. The maximum reflection loss reaches −31.6 dB at 17 GHz for the absorber in a thin thickness of 1.4 mm. As an additive for microwave absorbent, the tadpole-shaped (Ni, Al)/AlN nanoparticles can complement the deficiencies of high frequency loss to the traditional absorbents, and moreover, the chemical stability of aluminum nitride would allow the nanocomposite working in severe environmental conditions beyond the endurance of pure metals.

ACKNOWLEDGMENT

The authors acknowledge the support from National Basic Research Program of China (Grant No. 2011CB936002), National Natural

Science Foundation of China (NSFC 50801008), the project sponsored by SRF for ROCS, SEM ([2007] 1108) and the Second-Phase of BK (Brain Korea) 21 project.

REFERENCES

1. Wallace, J. L., "Broadband magnetic microwave absorbers: Fundamental limitations," *IEEE Trans. Magn.*, Vol. 29, 4209–4214, 1993.
2. Liu, X. G., D. Y. Geng, H. Meng, P. J. Shang, and Z. D. Zhang, "Microwave-absorption properties of ZnO-coated iron nanocapsules," *Appl. Phys. Lett.*, Vol. 92, 173117, 2008.
3. Zhen, L., Y. X. Gong, J. T. Jiang, C. Y. Xu, W. Z. Shao, P. Liu, and J. Tang, "Synthesis of $CoFe/Al_2O_3$ composite nanoparticles as the impedance matching layer of wideband multilayer absorber," *J. Appl. Phys.*, Vol. 109, 07A332, 2011.
4. Che, R. C., L. M. Peng, X. F. Duan, Q. Chen, and X. L. Liang, "Microwave absorption enhancement and complex permittivity and permeability of Fe encapsulated within carbon nanotubes," *Adv. Mater.*, Vol. 16, 401–405, 2004.
5. Bayrakdar, H., "Complex permittivity, complex permeability and microwave absorption properties of ferrite-paraffin polymer composites," *J. Magn. Magn. Mater.*, Vol. 323, 1882–1885, 2011.
6. Rajesh, S., V. S. Nisa, K. P. Murali, and R. Ratheesh, "Microwave dielectric properties of PTFE/rutile nanocomposites," *J. Alloys Compd.*, Vol. 477, 677–682, 2009.
7. Kim, J. H. and S. S. Kim, "Microwave absorbing properties of Ag-coated Ni-Zn ferrite microspheres prepared by electroless plating," *J. Alloys Compd.*, Vol. 509, 4399–4403, 2011.
8. Paula, R. K., K. H. Leeb, B. T. Lee, and H. Y. Song, "Formation of AlN nanowires using Al powder," *Mater. Chem. Phys.*, Vol. 112, 562–565, 2008.
9. Ambacher, O., "Growth and applications of group III-nitrides," *J. Phys. D: Appl. Phys.*, Vol. 31, 2653–2710, 1998.
10. Yin, L. W., Y. Bando, Y. C. Zhu, M. S. Li, Y. B. Li, and D. Golberg, "Growth and field emission of hierarchical single-crystalline wurtzite AlN nanoarchitectures," *Adv. Mater.*, Vol. 17, 110–114, 2005.
11. Liu, C., Z. Hu, Q. Wu, X. Z. Wang, Y. Chen, H. Sang, J. M. Zhu, S. Z. Deng, and N. S. Xu, "Vapor-solid growth and

characterization of aluminum nitride nanocones," *J. Am. Chem. Soc.*, Vol. 127, 1318–1322, 2005.

12. Shen, L. H., T. M. Cheng, L. J. Wu, X. F. Li, and Q. L. Cui, "Synthesis and optical properties of aluminum nitride nanowires prepared by arc discharge method," *J. Alloys Compd.*, Vol. 465, 562–566, 2008.
13. González, M. and A. Ibarra, "The dielectric behaviour of commercial polycrystalline aluminium nitride," *Diamond Relat. Mater.*, Vol. 9, 467–471, 2000.
14. Mikijelj, B., D. K. Abe, and R. Hutcheon, "AlN-based lossy ceramics for high average power microwave devices: Performance-property correlation," *J. Eur. Ceram. Soc.*, Vol. 23, 2705–2709, 2003.
15. Dong, X. L., Z. D. Zhang, X. G. Zhao, Y. C. Chuang, S. R. Jin, and W. M. Sun, "Characterization of Fe-Ni(C) nanocapsules synthesized by arc discharge in methane," *J. Mater. Res.*, Vol. 14, 1782–1790, 1999.
16. Yusoff, A. N., M. H. Abdullah, S. H. Ahmad, S. F. Jusoh, A. A. Mansor, and S. A. A. Hamid, "Electromagnetic and absorption properties of some microwave absorbers," *J. Appl. Phys.*, Vol. 92, 876–882, 2002.
17. Thapa, R., B. Saha, and K. K. Chattopadhyay, "Synthesis of cubic aluminum nitride by VLS technique using gold chloride as a catalyst and its optical and field emission properties," *J. Alloys Compd.*, Vol. 475, 373–377, 2009.
18. Joo, H. U., B. K. Min, and W. S. Jung, "Characteristics of aluminum nitride nanowhiskers grown via the vapor-liquid-solid mechanism," *Physica E*, Vol. 40, 833–835, 2008.
19. Petrov, I., E. Mojab, R. C. Powell, and J. E. Greene, "Synthesis metastable epitaxial zinc-blende-structure AlN by solid-state reaction," *Appl. Phys. Lett.*, Vol. 60, 2491–2493, 1992.
20. Wehner, A., Y. Jeliazova, and R. Franchy, "Growth and oxidation of a Ni_3Al alloy on Ni(1 0 0)," *Surf Sci.*, Vol. 531, 287–294, 2003.
21. Berzina, B., L. Trinkler, D. Jakimovica, V. Korsaks, J. Grabis, I. Steins, E. Palcevskis, S. Bellucci, L. C. Chen, S. Chattopadhyay, and K. H. Chen, "Spectral characterization of bulk and nanostructured aluminum nitride," *J. Nanophoton.*, Vol. 3, 031950, 2009.
22. Youngman, R. A. and J. H. Harris, "Luminescence studies of oxygen-related defects in aluminum nitride," *J. Am. Ceram. Soc.*, Vol. 73, 3238–3246, 1990.

23. Lu, B., X. L. Dong, H. Huang, X. F. Zhang, X. G. Zhu, J. P. Lei, and J. P. Sun, "Microwave absorption properties of the core/shell-type iron and nickel nanoparticles," *J. Magn. Magn. Mater.*, Vol. 320 1106–1111, 2008.
24. Gong, Y. X., L. Zhen, J. T. Jiang, C. Y. Xu, and W. Z. Shao, "Preparation of CoFe alloy nanoparticles with tunable electromagnetic wave absorption performance," *J. Magn. Magn. Mater.*, Vol. 321, 3702–3705, 2009.
25. Yan, S. J., L. Zhen, C. Y. Xu, J. T. Jiang, and W. Z. Shao, "Microwave absorption properties of $FeNi_3$ submicrometre spheres and SiO_2@$FeNi_3$ core-shell structures," *J. Phys. D: Appl. Phys.*, Vol. 43, 245003, 2010.
26. Banerjee, R., P. Ayyub, G. B. Thompson, R. Chandra, P. Taneja, and H. L. Fraser, "Microstructure and magnetic, transport, and optical properties of ordered and disordered Ni-25Al alloy thin films," *Thin Solid Films*, Vol. 441, 255–260, 2003.
27. He, J. H., R. Yang, Y. L. Chueh, L. J. Chou, L. J. Chen, and Z. L. Wang, "Aligned AlN nanorods with multi-tipped surfaces — Growth, field-emission, and cathodoluminescence properties," *Adv. Mater.*, Vol. 18, 650–654, 2006.
28. Michaelson, H. B., "The work function of the elements and its periodicity," *J. Appl. Phys.*, Vol. 48, 4729–4733, 1977.
29. Chew, W. C. and P. N. Sen, "Dielectric enhancement due to electrochemical double layer: Thin double layer approximation," *J. Chem. Phys.*, Vol. 77, 4683–4693, 1982.
30. Muñoz, R. D., A. L. Shluger, and G. Bersuker, "Ab initio study of charge trapping and dielectric properties of Ti-doped HfO_2," *Phys. Rev. B*, Vol. 79, 035306, 2009.
31. Kasu, M. and N. Kobayashi, "Large and stable field-emission current from heavily Si-doped AlN grown by metalorganic vapor phase epitaxy," *Appl. Phys. Lett.*, Vol. 76, 2910–2912, 2000.
32. Ravindran, R., K. Gangopadhyay, S. Gangopadhyay, N. Mehta, and N. Biswas, "Permittivity enhancement of aluminum oxide thin films with the addition of silver nanoparticles," *Appl. Phys. Lett.*, Vol. 89, 263511, 2006.
33. Thakur, A., P. Thakur, and J. H. Hsu, "Novel magnetodielectric nanomaterials with matching permeability and permittivity for the very-high-frequency applications," *Scripta. Mater.*, Vol. 64, 205–208, 2011.
34. Zhao, H. and H. H. Baua, "The polarization of a nanoparticle surrounded by a thick electric double layer," *J. Colloid Interf.*

Sci., Vol. 333, 663–671, 2009.

35. Zhou, R. H., H. C. Changa, V. Protasenko, M. Kuno, A. K. Singh, D. Jena, and H. L. Xing, "CdSe nanowires with illumination-enhanced conductivity: Induced dipoles, dielectrophoretic assembly, and field-sensitive emission," *J. Appl. Phys.*, Vol. 101, 73704, 2007.
36. Seo, D.-W., H.-J. Kim, K.-U Bae, and N.-H. Myung, "The effect of fiber orientation distribution on the effective permittivity of fiber composite materials," *Journal of Electromagnetic Waves and Applications*, Vol. 24, Nos. 17–18, 2419–2430, 2010.
37. Chen, Y. J., F. Zhang, G. G. Zhao, X. Y. Fang, H. B. Jin, P. Gao, C. L. Zhu, M. S. Cao, and G. Xiao, "Synthesis, multi-nonlinear dielectric resonance, and excellent electromagnetic absorption characteristics of Fe_3O_4/ZnO core/shell nanorods," *J. Phys. Chem. C*, Vol. 114, 9239–9244, 2010.
38. Wu, M. Z., Y. D. Zhang, S. Hui, T. D. Xiao, S. H. Ge, W. A. Hines, J. I. Budnick, and G. W. Taylor, "Microwave magnetic properties of $Co_{50}/(SiO_2)_{50}$ nanoparticles," *Appl. Phys. Lett.*, Vol. 80, 4404–4406, 2002.
39. Mercier, D., J.-C. S. Lévy, G. Viau, F. Fiévet-Vincent, F. Fiévet, P. Toneguzzo, and O. Acher, "Magnetic resonance in spherical Co-Ni and Fe-Co-Ni particles," *Phys. Rev. B*, Vol. 62, 532–544, 2000.
40. Naito, Y. and K. Suetake, "Application of ferrite to electromagnetic wave absorber and its characteristics," *IEEE T. Microw. Theory*, Vol. 19, 65–72, 1971.
41. Inui, T., K. Konishi, and K. Oda, "Fabrications of broad-band RF-absorber composed of planar hexagonal ferrites," *IEEE T. Magn.*, Vol. 35, 3148–3150, 1999.
42. Micheli, D., R. Pastore, C. Apollo, M. Marchetti, G. Gradoni, V. M. Primiani, and F. Moglie, "Broadband electromagnetic absorbers using carbon nanostructure-based composites," *IEEE T. Microw. Theory*, 2011, Doi: 10.1109/TMTT.2011.2160198.